Supporting Information

Multiscale Binder Engineering Enables High-Kinetics Prussian Blue Analogues Cathodes for Aqueous Na-Ion Batteries

Lizhang Yang[a], Jiayi Tang[a], Peng Zhao[a], Cai Liu[a], Daniel Mandler[b], Keun-il Kim[c], XiFeng Xia[a] , Zi-Han Zhao[d], Wu Lei*[a], Qiubo Guo*[a] and Qingli Hao*[a]

[a]Key Laboratory for Soft Chemistry and Functional Materials; School of Chemistry and Chemical Engineering, Nanjing University of Science and Technology, Ministry of Education, Nanjing 210094, Jiangsu, China

[b]Institute of Chemistry, Hebrew University of Jerusalem, Jerusalem 9190401, Israel

[c]School of Chemical, Biological and Battery Engineering, Gachon University, Seongnam-si,

[d]School of Chemistry and Chemical Engineering, Nanjing University of Science and Technology, Ministry of Education, Nanjing 210094, Jiangsu, China

Gyeonggi-do, 13120, Republic of Korea

*Corresponding authors.

mail: qinglihao@njust.edu.cn (Qingli Hao); qbguo@njust.edu.cn (Qiubo Guo); leiwuhao@njust.edu.cn (Wu Lei)

Synthesis of CoHCF

The synthesis of CoHCF followed a procedure analogous to that of NiHCF[1]. Solution A was prepared by dissolving 2 mmol of $CoCl_2 \cdot 6H_2O$ (Analytical Reagent, Macklin) and 7 mmol of sodium citrate in 100 mL of deionized water. Separately, Solution B was prepared by dissolving 14 g NaCl (>99.5%, Aladdin) and 2 mmol of $Na_4[Fe(CN)_6] \cdot 10H_2O$ in 100 mL of deionized water. After both solutions were individually stirred for a while, Solution A was added dropwise into Solution B under continuous stirring. The resulting mixture was stirred for 24 h. The product was isolated by centrifugation, washed thoroughly, and dried to yield CoHCF.

Preparation of Binder Film

The binder film was prepared in the same way as the electrode, with the only difference being that no other substances were added.

Materials Characterization

The crystal structure of materials was characterized by X-ray diffraction (XRD, Bruker-AXS D8 Advance). The hydrophilic properties of the electrodes were determined via contact angle measurement (V1, Yunfan Instrument, China). Unless otherwise specified, the contact angle tests were conducted using 17 m sodium perchlorate as the electrolyte, with a consistent droplet volume of 11-12 μL used for each measurement. All contact angle experiments were performed with the same injector under identical testing conditions and procedures to ensure data validity. Adhesion tests were performed on a universal tensile tester (AGS-X, Shimadzu, Japan) using alumina ceramic sheets as substrates, with a tensile speed of 2 mm min^{-1}.Mesoscale morphology of electrodes was analyzed using field-emission scanning electron microscopy (SEM, JSM-7800F PRIME). Three-dimensional mesostructures of electrodes were reconstructed via X-ray microscopy (Zeiss Xradia 515 Versa). Functional group variations were resolved by Fourier-transform infrared spectroscopy (FTIR, Bruker) with germanium attenuated total reflectance

(ATR) crystal. Electrodes composition was determined by thermogravimetric analysis (TGA 5500) under nitrogen atmosphere at a heating rate of 10°C min^{-1}.

We employed a gravimetric uptake method to preliminarily investigate the wettability of electrolytes in different electrodes. Specifically, electrode films were cut into 1 cm^2 pieces and weighed. Then, 50 μL of electrolyte was pipetted onto each electrode surface. After standing at room temperature for 30, 60, 90, and 120 minutes, the surface electrolyte was removed using the same method. The electrodes were thoroughly dried and reweighed. The mass difference before and after the process represents the mass increase.

DFT calculation methods

All density functional theory (DFT) calculations were performed within the Vienna Ab initio Simulation Package (VASP) framework[2]. Exchange-correlation effects were modeled using the Perdew-Burke-Ernzerhof (PBE) generalized gradient approximation (GGA)[3], while dispersion interactions were addressed through the semi-empirical DFT-D3 correction[4]. The projected augmented wave (PAW) method with a 450 eV plane-wave energy cutoff treated core-valence electron interactions. Brillouin zone sampling employed a 4 × 4 × 1k-point grid during geometry optimizations, with convergence thresholds set at 0.02 eV $Å^{-1}$ for atomic forces and 1×10^{-5} eV for total energy. To eliminate spurious interlayer interactions, a >15 Å vacuum region was applied normal to the interface along the z-direction. Post-processing operations, including three-dimensional band structure computation and visualization, were executed using VASPKIT[5].

Cells assembly and electrochemical measurements

All cells were assembled in air using three-electrode Swagelok® cells. For half-cell assemble, unless otherwise specified, the test electrode served as the working electrode, an activated carbon PTFE electrode film as the counter electrode, and an Ag/AgCl reference electrode, with 17 M $NaClO_4$ as the electrolyte. In full cells, the mass ratio of NiHCF to AC was consistently 1:2. For full cells using PTFE electrode films, the positive electrodes loading were 8-10 mg cm^{-2}, while for those using 3D-printing electrodes, the positive electrode loading was 20-24 mg cm^{-2}. Glass fiber (Whatman GF/D, diameter = 12 mm) was used as the separator in all cases.

Galvanostatic charge-discharge (GCD), rate capability tests, and Galvanostatic Intermittent Titration Technique (GITT) were performed on a Land CT2001A battery tester. Cyclic voltammetry (CV) and electrochemical impedance spectroscopy (EIS) measurements were conducted on a CHI760e electrochemical workstation. Unless otherwise specified, the CV tests were carried out within a voltage range of 0-1.2 V *vs* Ag/AgCl. For EIS tests, the frequency range was from 1 MHz to 0.01 Hz with an applied amplitude of 10 mV, acquiring 10 data points per

decade. Distribution of Relaxation Times (DRT) analysis was performed using a MATLAB GUI toolbox developed by the Ciucci research team6. Unless otherwise stated, all electrochemical tests were carried out at a constant temperature of 26 °C.

GITT was employed to investigate the kinetics of charge carrier diffusion during the process. A current density of 0.1 A g^{-1} was applied, with current pulses of 90 seconds during charge/discharge and an open-circuit rest time of 2 minutes. The apparent diffusion coefficient (D_{Na^+}>) of Na^+ ions within the NiHCF electrode was calculated using the following equation:

$$D = \frac{4}{\pi\tau}\left(\frac{m_B V_M}{M_B S}\right)^2\left(\frac{\Delta E_S}{\Delta E_\tau}\right)^2 \left(\tau \ll \frac{L^2}{D}\right)$$

Where: m_B, S and L represent the active material mass, area, and thickness of the electrode, respectively; M_B and V_M denote the molecular weight and molar volume of NiHCF; ΔE_S and ΔE_τ correspond to the potential changes during the current pulse at different times and the difference in steady-state potential changes at the plateau potential, respectively.

Supplementary Note1:

We acknowledge the valid concern regarding the use of N-Methyl-2-pyrrolidone (NMP) as the processing solvent for the polyvinylidene fluoride (PVDF) binder in this study. Although NMP is a conventional and highly effective solvent for fabricating high-performance PVDF-based electrodes—ensuring excellent binder dissolution, slurry rheology, and electrode adhesion—its application conflicts significantly with the overarching goals of green and scalable manufacturing. In subsequent work, building on our current research, we will systematically explore more environmentally friendly electrode manufacturing processes. This includes developing eco-friendly solvent systems compatible with PVDF, as well as investigating alternative binder systems that are suited to green processing without compromising electrochemical performance.

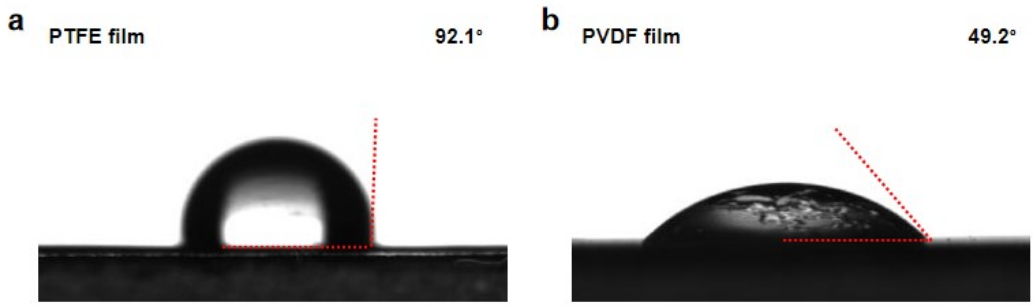

Fig. S1 Contact angle measurements for PTFE film and PVDF film.

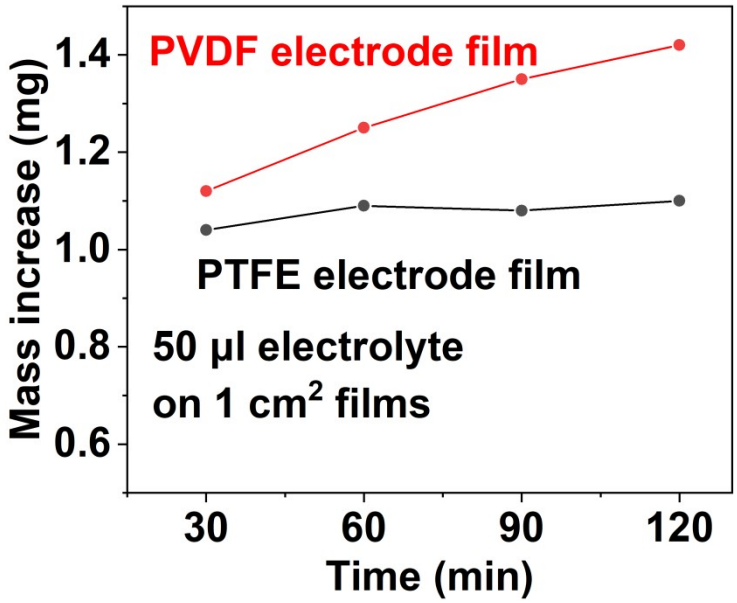

Fig. S2 Gravimetric uptake curves for PVDF electrode film and PTFE electrode film

Supplementary Note2:

The gravimetric uptake tests yielded results consistent with the contact angle measurements: the electrolyte continuously infiltrated the PVDF electrode film, leading to a significant mass increase (1.12 mg for PVDF vs. 1.04 mg for PTFE at 30 minutes). This mass gain for the PVDF electrode continued to grow over the two-hour period, reaching 1.25 mg, 1.35 mg, and 1.42 mg at 60, 90, and 120 minutes, respectively. In contrast, the mass of the PTFE electrode film remained around 1.09 mg after 60 minutes. These results confirm the superior and sustained electrolyte permeation in the PVDF electrode film, which facilitates the establishment of efficient ion transport networks within the electrode.

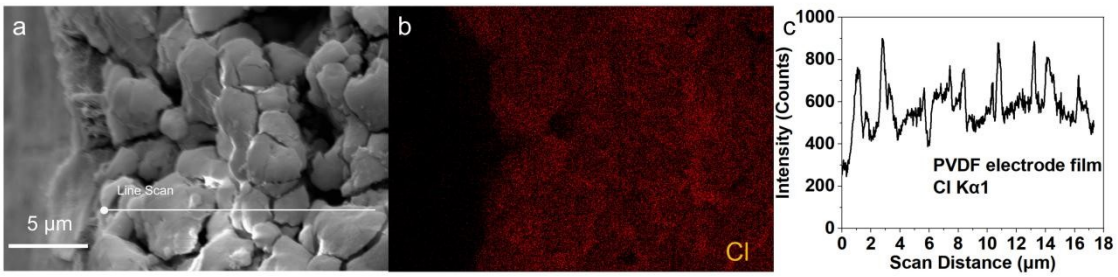

Fig. S3 (a) Cross-sectional SEM image of the PVDF electrode film. (b) EDS elemental mapping of Cl. (c) Line scanning data of Cl.

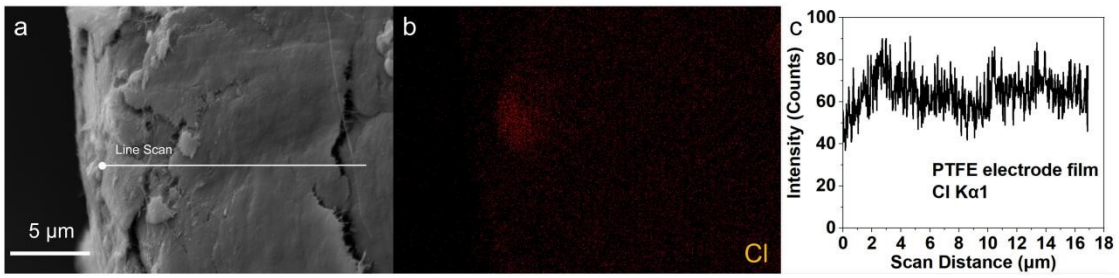

Fig. S4 (a) Cross-sectional SEM image of the PTFE electrode film. (b) EDS elemental mapping of Cl. (c) Line scanning data of Cl.

Supplementary Note3:

We employed EDS elemental mapping and line scanning to analyze the cross-sectional distribution of Cl in the electrode sheets after mass tracking experiments. Chlorine is exclusively present in the electrolyte and absent in the pristine electrodes. The results indicate that a certain amount of Cl is detected in both PTFE and PVDF electrode films. However, the Cl content in the PVDF electrode film (Fig. S11 (b), (c)) is significantly higher than that in the PTFE electrode film (Fig. S12 (b), (c)). This suggests that electrolyte penetration occurs in both types of electrode films, but the PVDF electrode film exhibits superior permeability. These findings are consistent with our previous contact angle measurements and mass tracking experimental results.

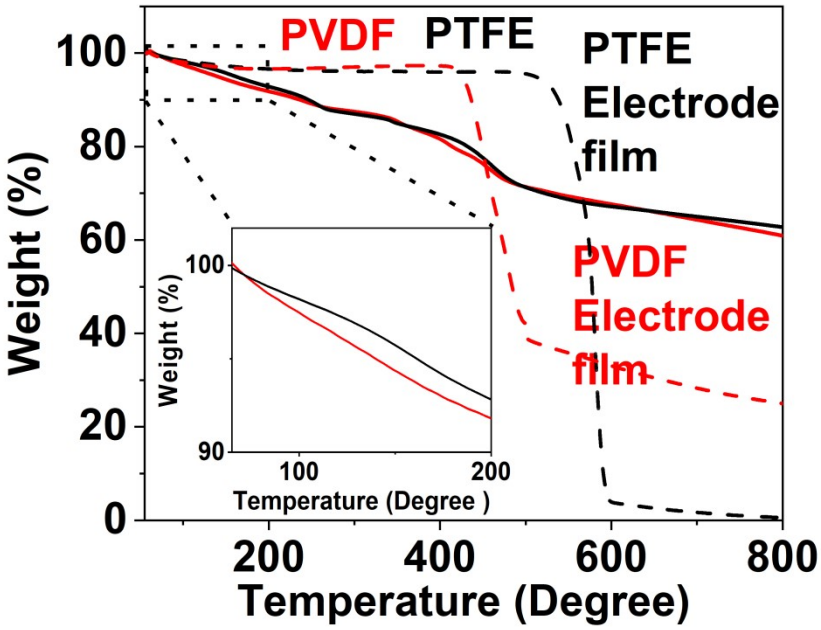

Fig. S5 TGA graph of PVDF、PTFE、PVDF electrode film and PTFE electrode film in a nitrogen atmosphere.

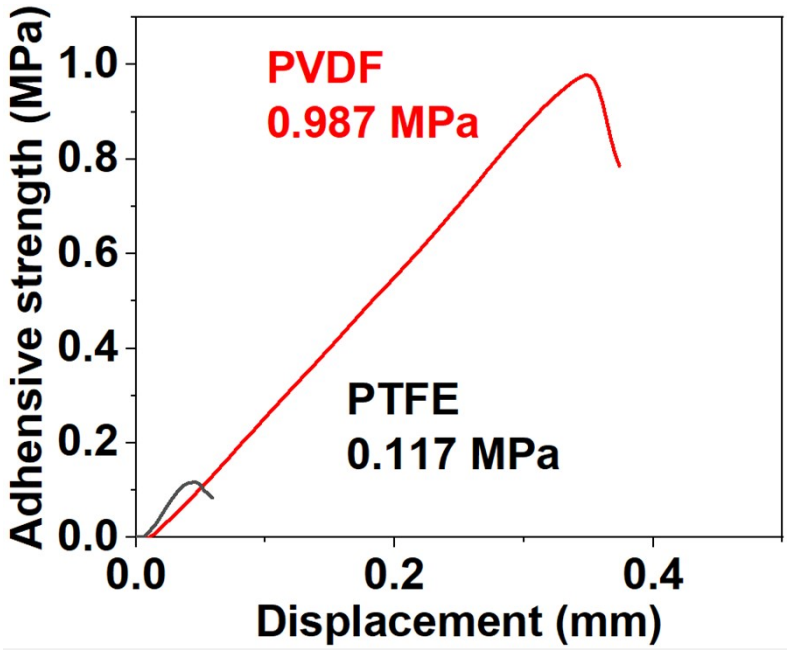

Fig. S6 Adhesion strength of PVDF and PTFE.

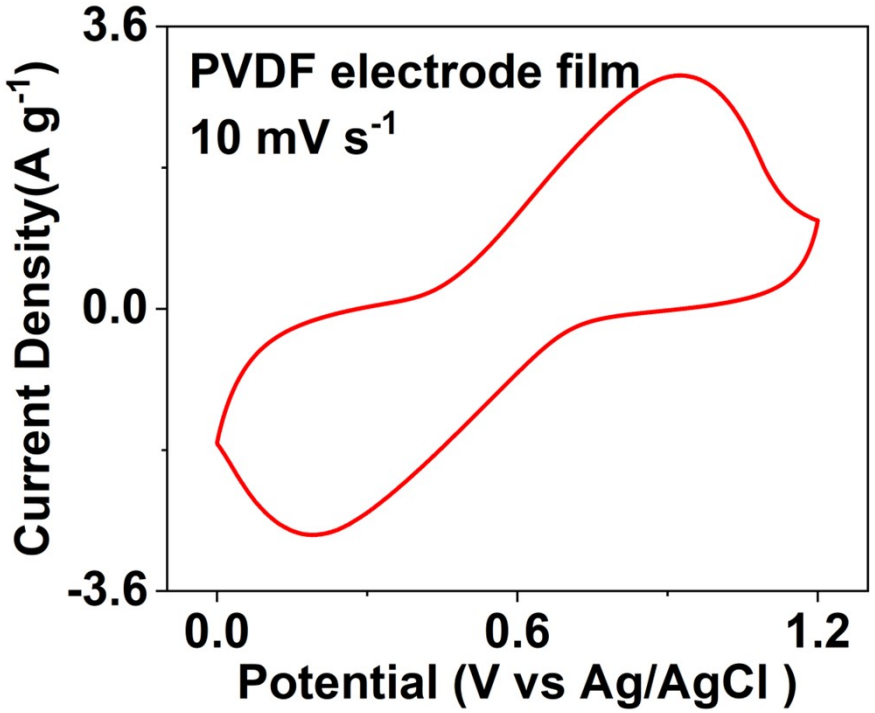

Fig. S7 CV curve of PVDF film electrode at 10 mV s^{-1}.

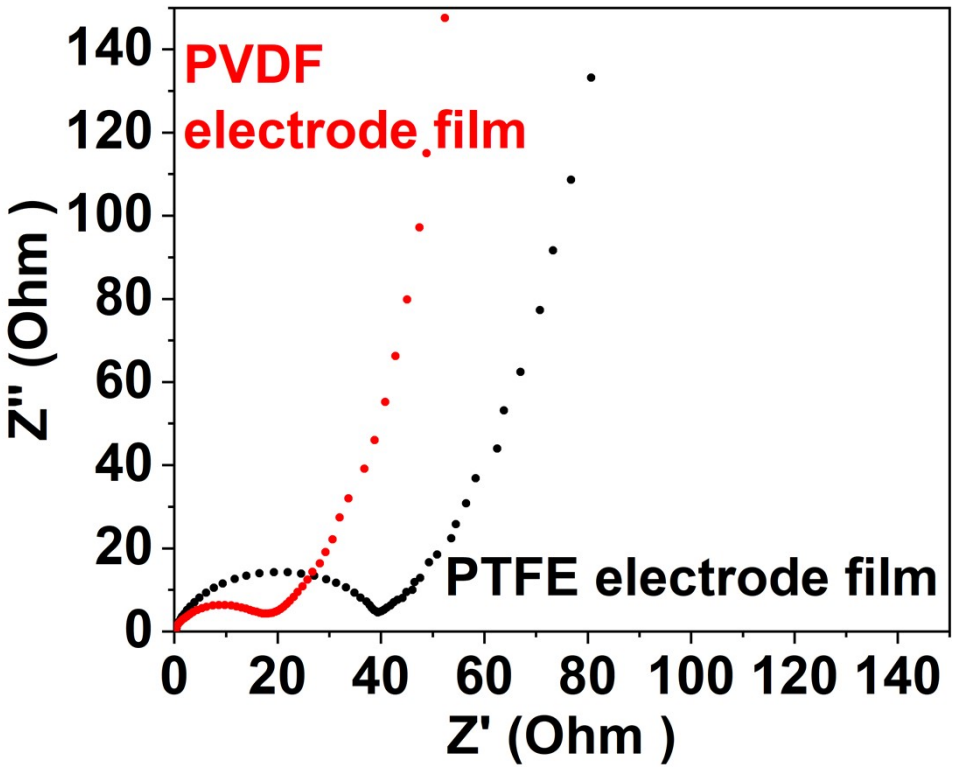

Fig. S8 Nyquist plots of PVDF electrode film and PTFE electrode film.

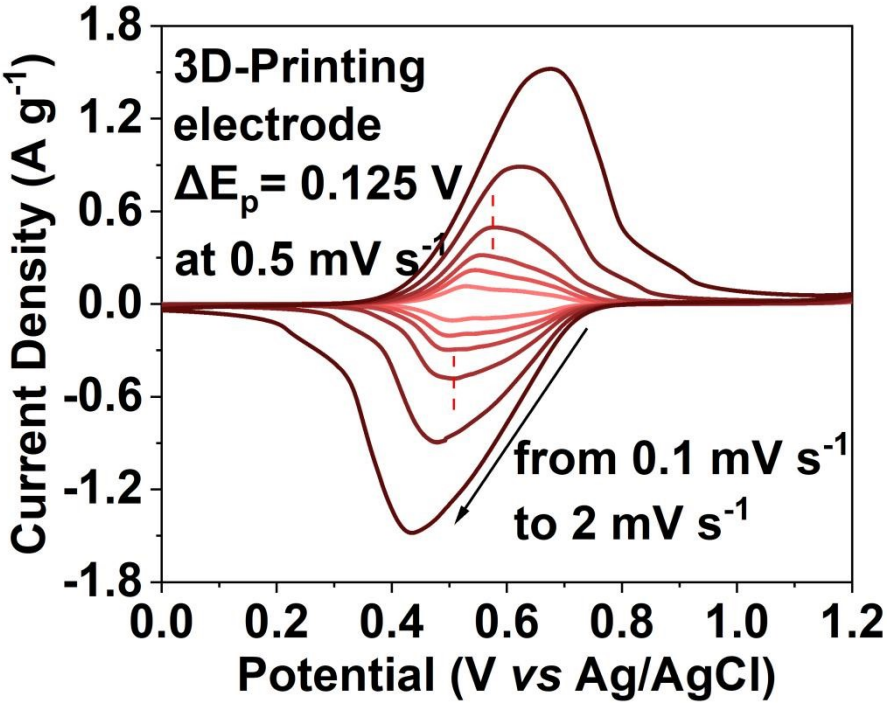

Fig. S9 CV curve of 3D-printing electrode from 0.1 to 2 mV s^{-1}.

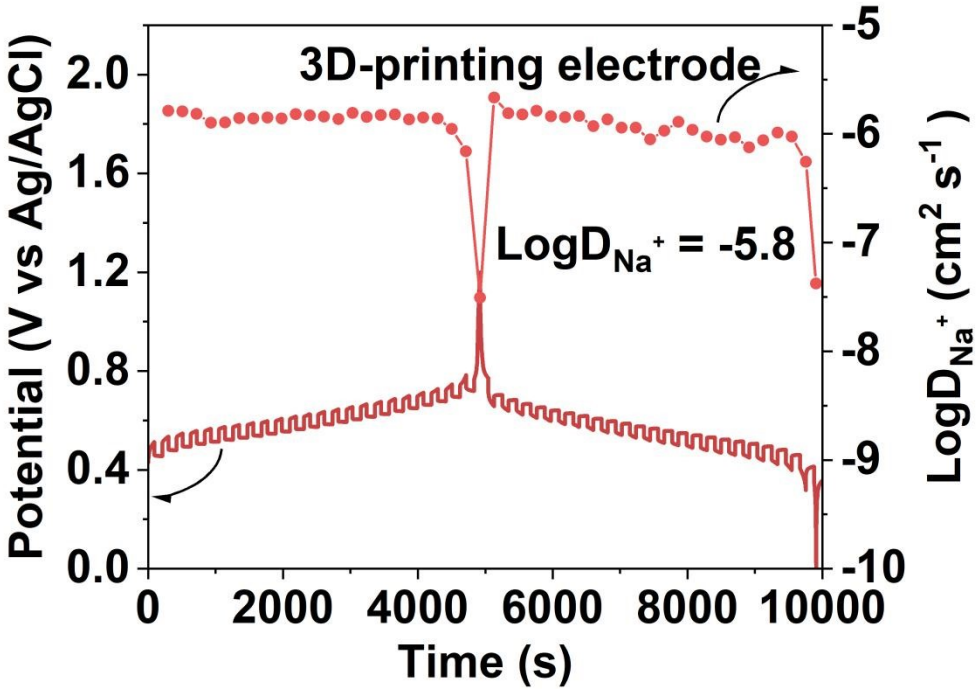

Fig. S10 Discharge-charge GITT plots at 0.1 A g^{-1} of 3D-printing electrode.

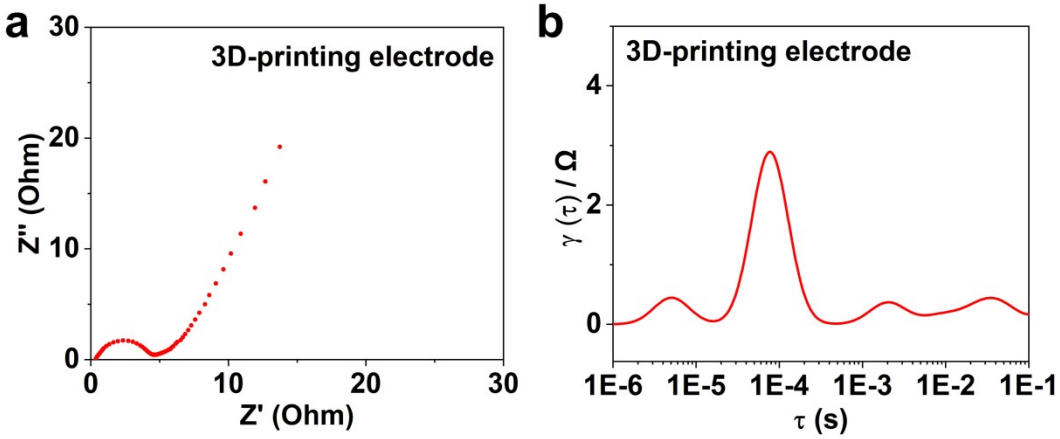

Fig. S11 (a) Nyquist plots of 3D-printing electrode. (b) DRT curves of 3D-printing electrode.

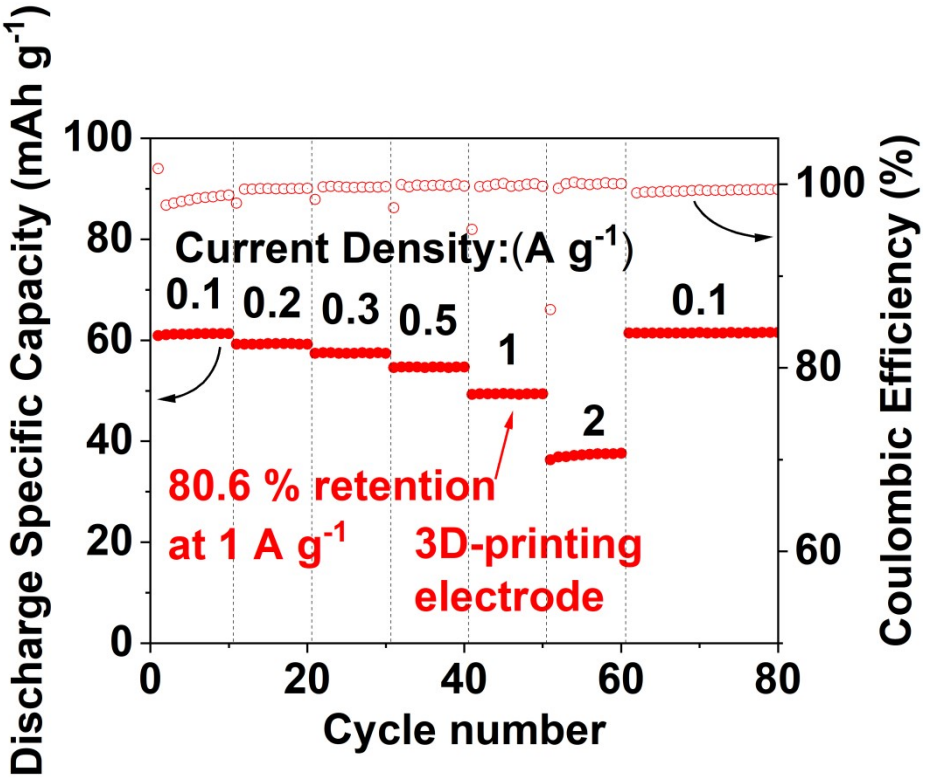

Fig. S12 Rate performance of 3D-printing electrode at the current density from 0.1 to 2 A g^{-1}.

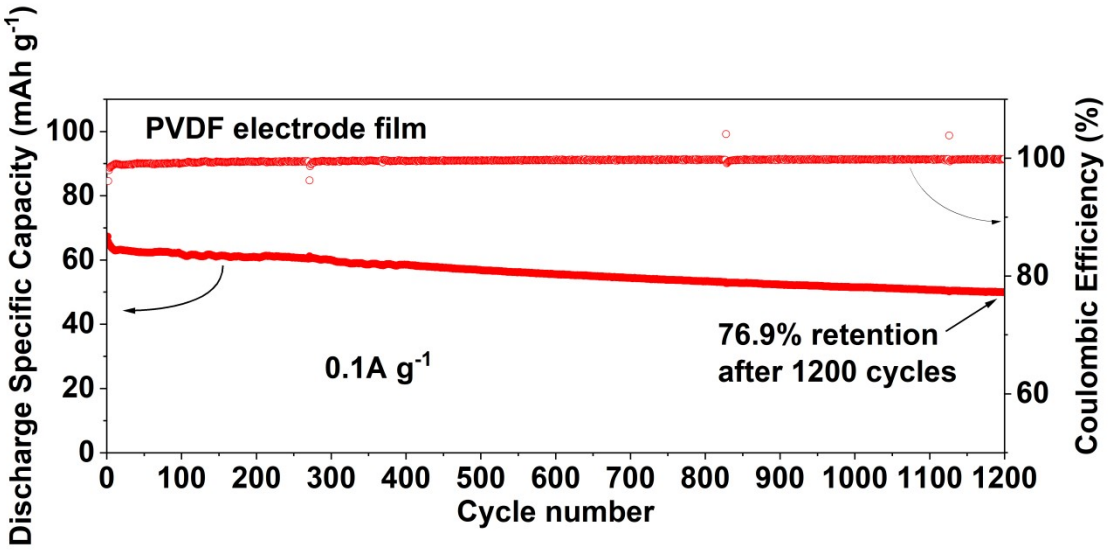

Fig. S13 Long-term cycling stability of PVDF electrode film at 0.1 A g^{-1}.

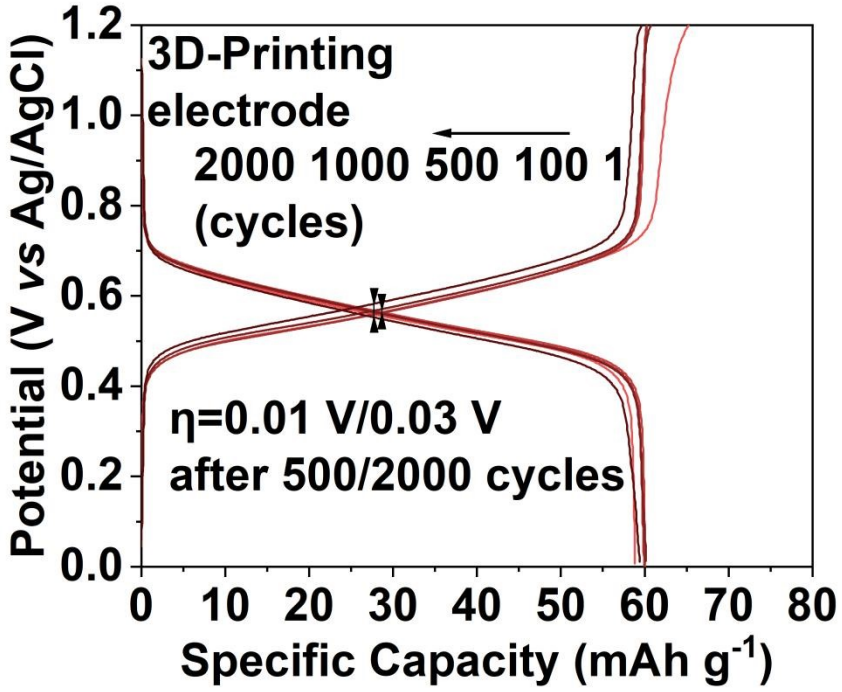

Fig. S14 The charge-discharge profiles of 3D-printing electrode film at 0.1 A g^{-1}

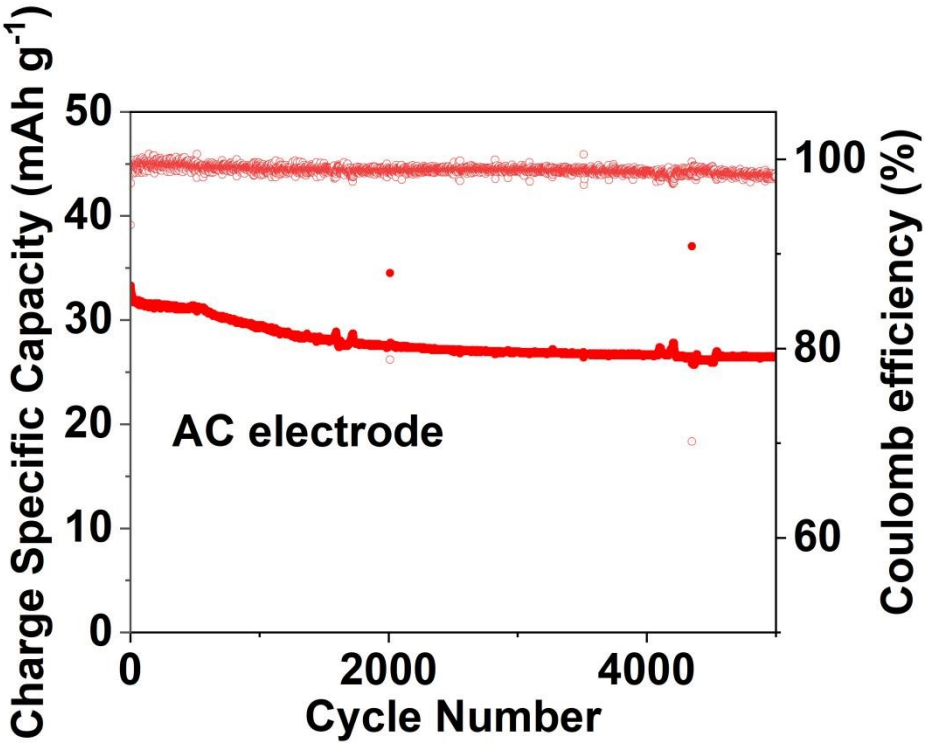

Fig. S15 Long-term cycling stability of AC electrode at 0.1A g^{-1} .

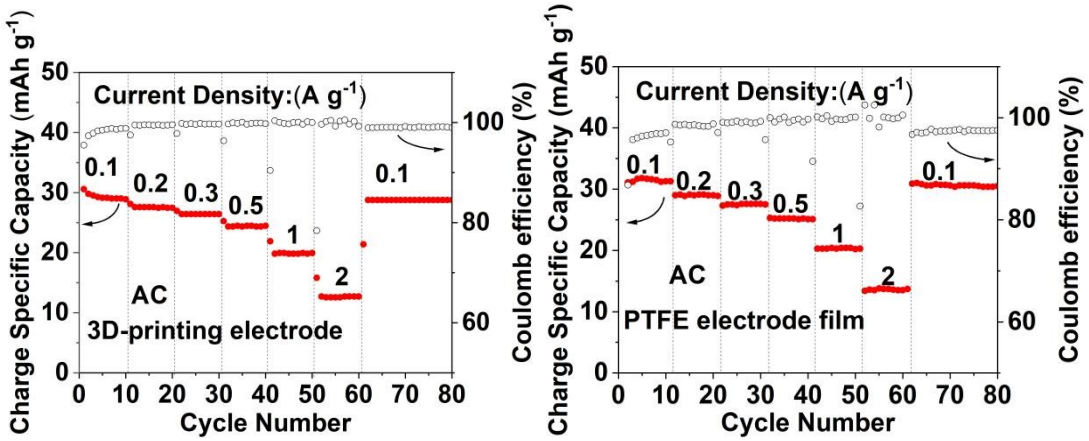

Fig. S16 Rate performance of AC electrode at the current density from 0.1 to 2 A g^{-1}.

Supplementary Note4:

Although the 3D-printing AC electrodes and PTFE electrode films exhibit very similar rate performance, the 3D-printing activated carbon electrodes still demonstrate higher Coulombic efficiency and smaller capacity fluctuations during cycling. This indicates that the 3D printing strategy can still bring certain improvements to the activated carbon anode.

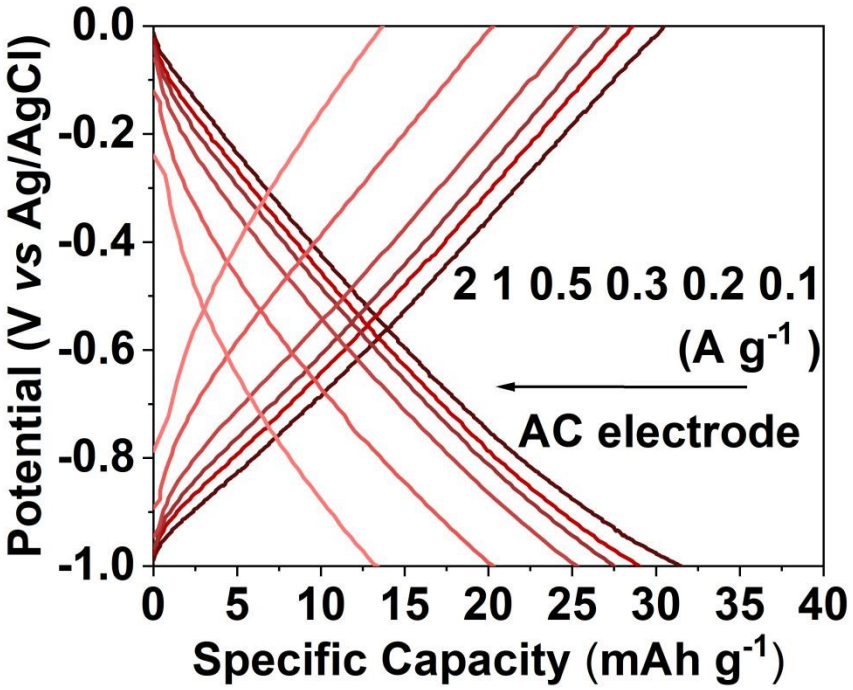

Fig. S17 The charge-discharge profiles of AC electrode from 0.1 to 2 A g^{-1}.

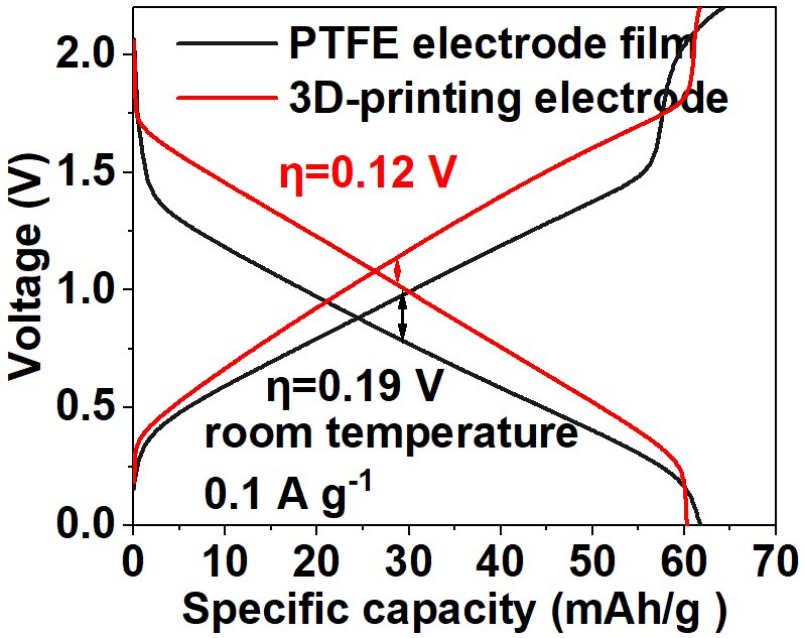

Fig. S18 The charge-discharge profiles of full cells (NiHCF//AC) at 0.1 A g^{-1} at room temperature.

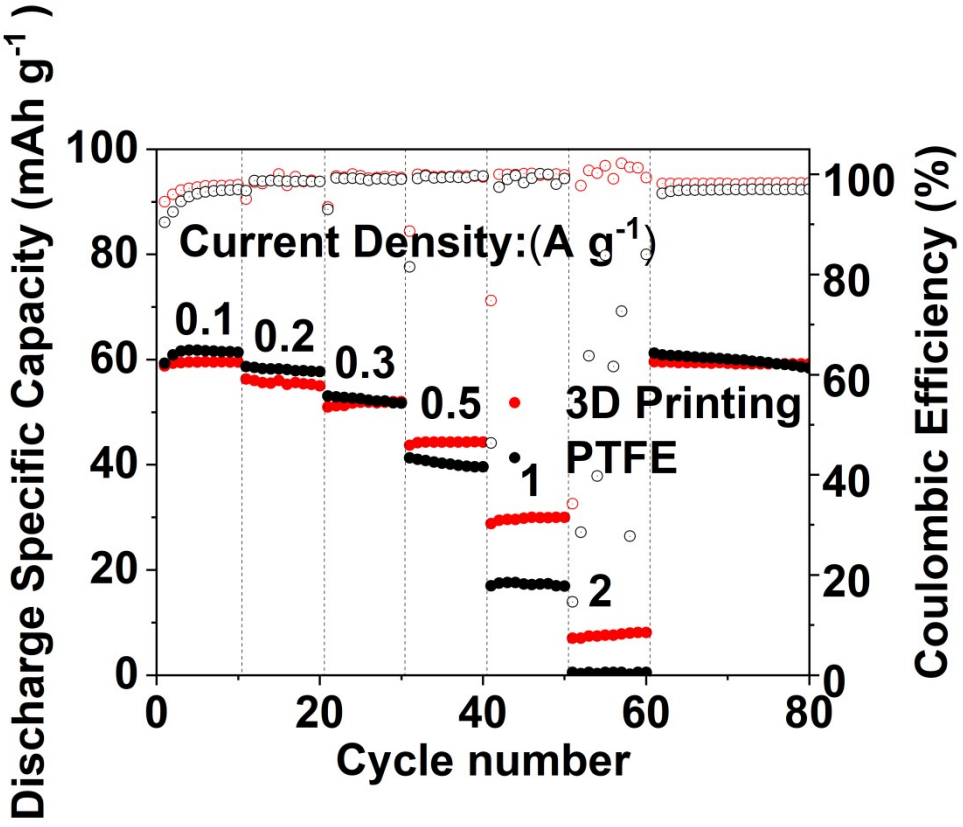

Fig. S19 Rate performance of full cells (NiHCF//AC) at the current density from 0.1 to 2 A g^{-1}.

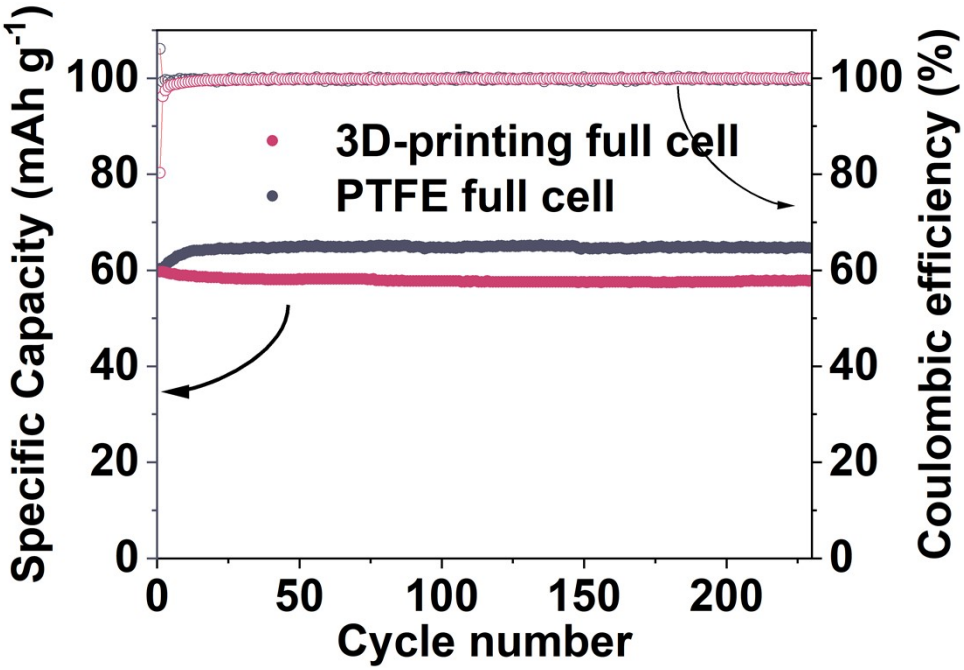

Fig. S20 Long-term cycling stability of full cells (NiHCF//AC) at 0.1A g^{-1} at -20°C.

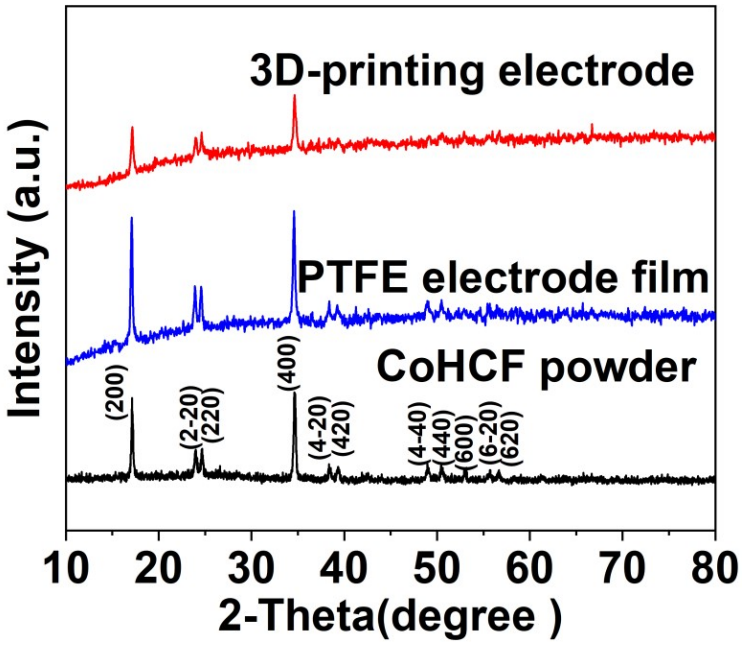

Fig. S21 XRD patterns of CoHCF powder and electrodes.

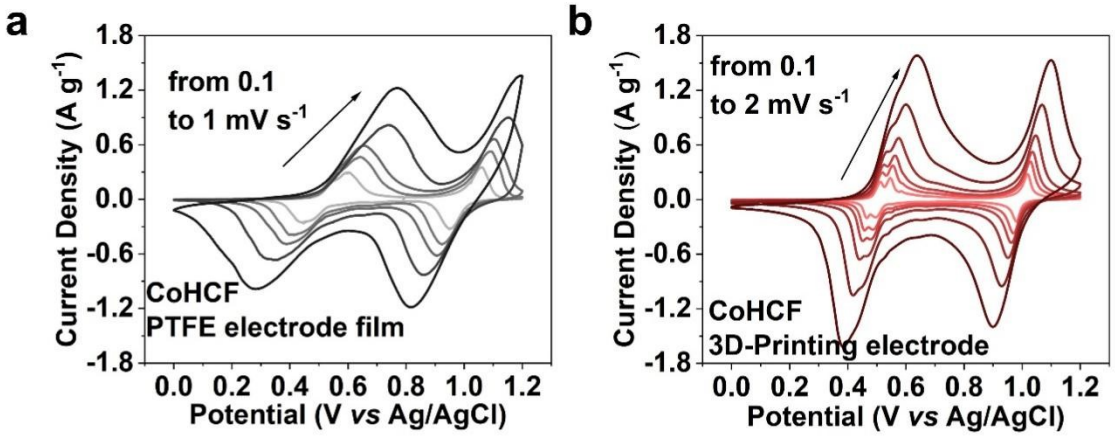

Fig. S22 CV curves of (a) PTFE electrode film from 0.1 to 1 mV s^{-1}, and (b) 3D-printing electrode from 0.1 to 2 mV s^{-1}.

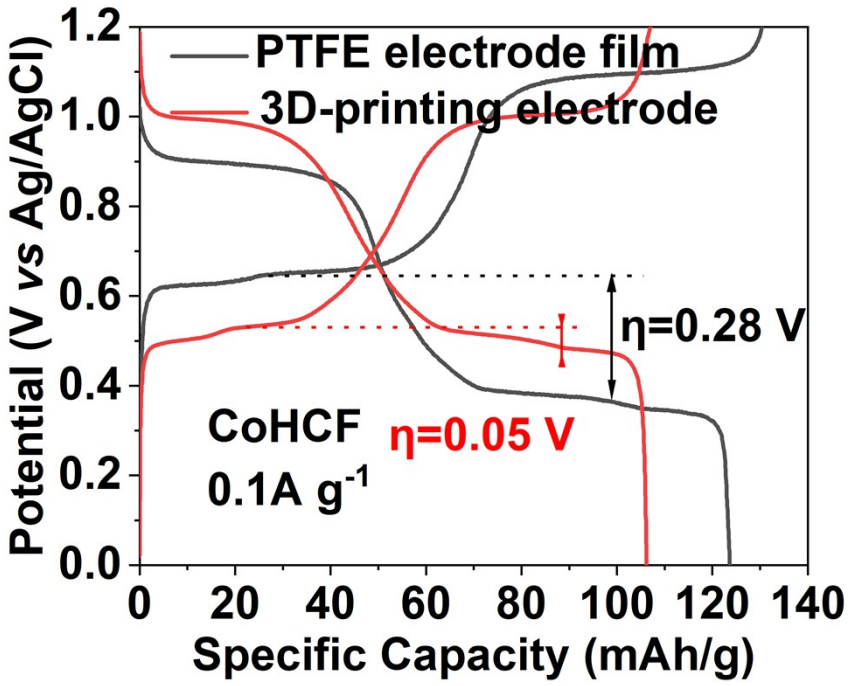

Fig. S23 The charge-discharge profiles of CoHCF PTFE electrode film and CoHCF 3D-printing electrode at 0.1 A g^{-1}.

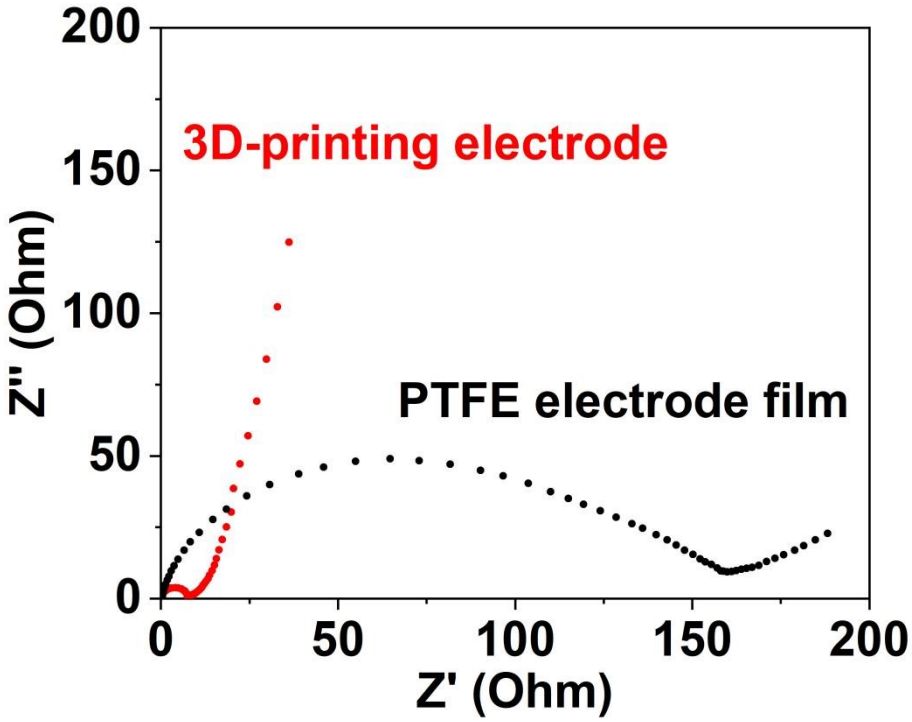

Fig. S24 Nyquist plots of 3D-printing electrode and PTFE electrode film of CoHCF.

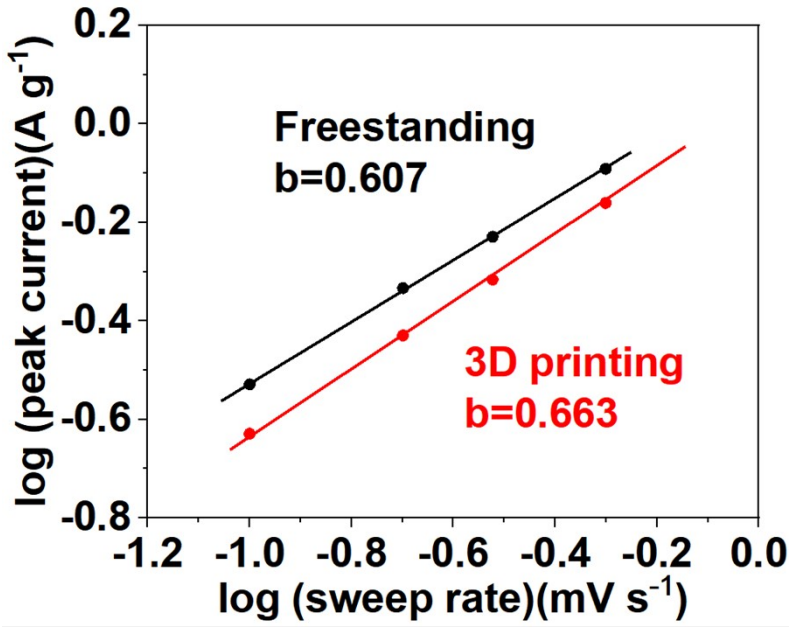

Fig. S25 b-Value of CoHCF electrodes.

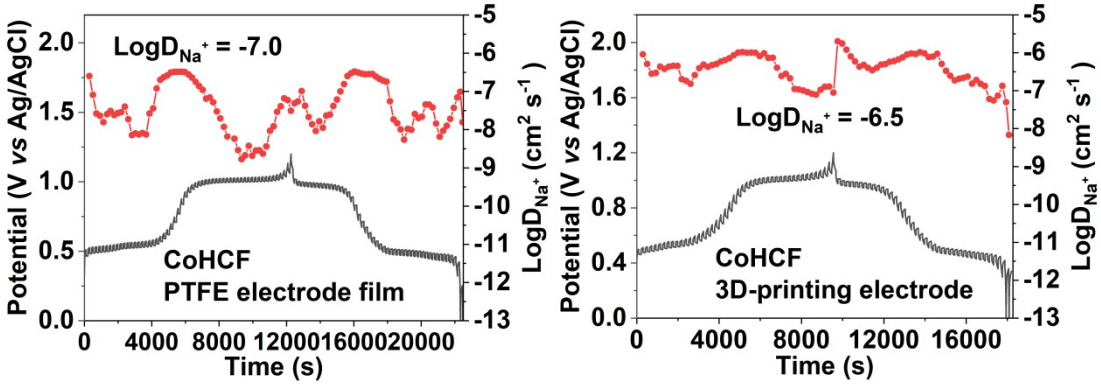

Fig. S26 Discharge-charge GITT plots at 0.1 A g^{-1} of CoHCF PTFE electrode film and CoHCF PVDF electrode film.

Table S1. Table comparing rate performance vs. mass loading with literature data.

Reference	Capacity retention	Massload	current collector
this work	90.0% at 0.5 A g^{-1}	20-24	current collector-free
Ref1, m-NiHCF[7]	98.0% at 0.5 A g^{-1}	not mentioned	current collector-integrated
Ref2, $Ni_{0.4}Co_{0.6}HCF$[8]	67.0% at 5 C	not mentioned	current collector-integrated
Ref3, NiHCF@CNT[9]	87.0% at 0.5 A g^{-1}	2-2.5	current collector-integrated
Ref4, Nafion-NiHCF[10]	89.0% at 0.4 A g^{-1}	not mentioned	current collector-integrated
Ref5, M5HCF[11]	88.8% at 0.5 A g^{-1}	2	current collector-integrated
Ref6, Nano-Ni/CoHCF[12]	82.0% at 0.5 A g^{-1}	not mentioned	current collector-integrated
Ref7, NiHCF-h[13]	94.0% at 0.5 A g^{-1}	5.5	current collector-integrated

Supplementary References

1 K. Zhu, Z. Li, Z. Sun, P. Liu, T. Jin, X. Chen, H. Li, W. Lu and L. Jiao, *Small*, 2022, **18**, 2107662.

2 G. Kresse and J. Furthmüller, Comput. *Mater. Sci*, 1996, **6**, 15-50.

3 J. P. Perdew, K. Burke and M. Ernzerhof, *Phys. Rev. Lett.*, 1996, **77**, 3865-3868.

4 S. Grimme, J. Antony, S. Ehrlich and H. Krieg, *J. Chem. Phys.*, 2010, **132**, 154104.

5 V. Wang, N. Xu, J.-C. Liu, G. Tang and W.-T. Geng, Comput. *Phys. Commun.*, **2021**, 267, 108033.

6 T. H. Wan, M. Saccoccio, C. Chen and F. Ciucci, *Electrochim. Acta.*, 2015, **184**, 483-499.

7 L. Shen, Y. Jiang, Y. Liu, J. Ma, T. Sun and N. Zhu, *Chem. Eng. J.*, 2020, **388**, 124228.

8 W. Li, F. Zhang, X. Xiang and X. Zhang, *J. Phys. Chem. C*, 2017, **121**, 27805-27812.

9 Y. Yuan, D. Bin, X. Dong, Y. Wang, C. Wang and Y. Xia, *ACS Sustainable Chem. Eng.*, 2020, **8**, 3655-3663.

10 H. Gu, Z. Lai, X. Wang, W. Sun, Y. Rong and F. Guo, J. Alloys Compd., 2025, 1026, 180419.

11 X. Zhao, Z. Xing and C. Huang, *J. Mater. Chem. A*, 2023, **11**, 22835-22844.

12 Y. Zeng, Y. Wang, Z. Huang, H. Luo, H. Tang, S. Dong and P. Luo, *Nanotechnology*, 2023, **34**, 475403.

13 Y. Xu, M. Ou, Y. Liu, J. Xu, X. Sun, C. Fang, Q. Li, J. Han and Y. Huang, *Nano Energy*, 2020, **67**, 104250.